Numerical Investigation of Heat Transfer and Flow Characteristics in Phase-Change Transpiration Cooling for Hypersonic Re-entry Vehicle

Junhyeon Bae*, Jukyoung Shin, Tae Young Kim Department of Mechanical and Automotive Engineering, Seoul National University of Science and Technology, 232 Gongneung-ro, Nowon-gu, Seoul 01811, Republic of Korea

Abstract

Effective thermal protection systems are critical for the viability of reusable space vehicles enduring extreme atmospheric re-entry heating. Among active cooling strategies, transpiration cooling using liquid coolants is particularly promising, but its performance is complicated by internal phase-change phenomena. This study presents a numerical investigation into coupled thermo-hydrodynamics within porous media, aiming to elucidate the underlying complex mechanisms of phase-change transpiration cooling. A high-precision numerical model, validated with existing literature, was developed to systematically analyse the effects of various heat fluxes and coolant mass flow rates on system performance. The steady-state results demonstrate that the system's thermal and hydrodynamic characteristics are intricately linked to the location of the internal phase change. The instability of phase-change cooling systems is identified, wherein the sharp decrease in average kinematic viscosity due to reduced vapor fraction outweighs the effect of increased mass flow rate, resulting in reduced pressure drop as flow rate increases. Temperature distribution analysis revealed steeper temperature gradients in the vapor region compared to the liquid region due to lower thermal conductivity, with pronounced local thermal non-equilibrium effects in the two-phase region.

Keywords: Transpiration cooling, Phase change, Two-phase mixture model, Local thermal non-equilibrium, Porous medium

Nomenclature

LatinSubscriptsK – Absolute permeabilityf – fluid m_f – Coolant mass fluxs – solidq'' – Heat fluxI – liquidh – Specific enthalpyv – vaporT – Temperatureeff – effectives – Liquid saturationsat – saturated

1. Introduction

1.1. Background

The necessity for developing fully reusable space vehicles is ever-increasing as a solution to drastically reduce launch costs, which are a key factor in determining the economic viability and sustainability of the aerospace industry [1]. However, the development of fully reusable spacecraft faces a fundamental technical challenge, which is the extreme aerodynamic heating phenomenon during atmospheric reentry. Upon completing a mission and re-entering the atmosphere, a space vehicle flies at speeds approaching Mach 20–25, strongly compressing the air in front of the vehicle and creating high-temperature shock waves. The formation of these shock waves and viscous heating effects within the boundary layer creates an extreme heat flux environment where stagnation point temperatures exceed 10,000K [2, 3]. Therefore, the implementation of effective thermal protection systems is essential to manage extreme thermal conditions and ensure vehicle survivability.

Thermal protection systems are broadly categorised into passive and active thermal protection systems [4]. Traditional passive thermal protection systems, such as conventional insulation tiles or hot structures, rely on the material properties themselves to withstand or dissipate heat, making them inherently vulnerable to degradation, including micro-cracking and coating damage [5, 6]. On the other hand, active cooling systems utilise the circulation or injection of gaseous or liquid coolants to actively

remove thermal energy, thereby cooling the structure's temperature below the material's permissible limits. Notably, film cooling, effusion cooling, and transpiration cooling share a similar operating principle: a coolant is ejected directly onto the hot surface, forming an insulating film that reduces the incoming heat flux from the high-temperature flow [7–9]. Unlike film or effusion cooling which rely on discrete jets, transpiration cooling's uniform coolant injection through a porous structure not only provides superior thermal efficiency with minimal coolant, but also enhances durability by mitigating issues like hotspots and surface degradation. Therefore, transpiration cooling is attracting much attention in the field of thermal management for hypersonic and reusable space vehicles due to its robust and efficient thermal protection capabilities.

1.2. Motivations

Recent research on transpiration cooling is broadly categorised by choice of coolant into gas-based [10] and liquid-based systems [11]. Liu et al. [10] conducted a comparative study of transpiration cooling performance using air, nitrogen, argon, carbon dioxide, and helium as coolants in a nose cone model made of sintered stainless steel particles. Their results revealed that helium provided the most effective cooling, which was attributed to its high specific heat. Meanwhile, liquid coolants inherently possess a higher specific heat capacity than gases, and further offer significant thermal advantages over gases by utilising latent heat during phase change to enhance cooling performance. The pivotal role of latent heat in enhancing transpiration cooling was demonstrated by Van Foreest et al. [11] in their comparative experiments between liquid water and gaseous nitrogen. They found that while a nitrogen gas flow rate five times higher could only lower the surface temperature to around 1500 K, a minimal 0.2 g/s of water, leveraging its phase change, plummeted the temperature from over 2000 K to below 500 K.

Despite the superior performance of liquid transpiration cooling, the phase change process introduces major challenges, including flow instabilities and vapor blockage caused by rapid volume expansion within the pores [12–16]. The rapid volumetric expansion can choke the fine pores, impeding the steady supply of liquid coolant to the hot surface and leading to a degradation of cooling performance. Experimental analysis of internal fluid behavior is inherently challenging due to the complex pore network, necessitating theoretical and numerical approaches to understand the intricate liquid-vapor interactions.

Numerical modeling of phase change in porous media has primarily evolved along two paths: Separated Phase Models (SPM) [17] and Two-Phase Mixture Models (TPMM) [18]. While SPM offers high fidelity, its prohibitive computational cost has driven the widespread adoption of the TPMM, a framework initially proposed by Wang and Beckerman [18]. In this approach, the multiphase flow is treated as a single pseudo-fluid, simplifying the governing equations. Based on the assumption that the high specific surface area in low-porosity media ensures intense heat transfer, the Local Thermal Equilibrium (LTE) model posits that fluid and solid temperatures are equal, thus simplifying the separate energy equations into a single, widely used formulation [19]. However, acknowledging the realistic existence of temperature differences between phases, researchers developed the Local Thermal Non-Equilibrium (LTNE) model to provide more accurate descriptions of heat transfer processes, with validation through comprehensive studies examining interfacial heat transfer coefficients [20–22]. The LTNE approach has been subsequently coupled with two-phase theoretical models, enabling researchers to conduct detailed examinations of the complex interplay between fluid flow, heat transfer, phase change mechanisms, and unsteady variations within transpiration cooling porous media [23–26].

1.3. Objective

Despite the established advantages of liquid-based transpiration cooling, a deeper understanding of the complex internal phenomena is crucial to overcome the challenges of phase change. Therefore, the primary objective of this study is to conduct a comprehensive numerical investigation into the coupled fluid flow, heat transfer, and phase-change mechanisms within a transpiration cooling system under re-entry conditions. To this end, a high-fidelity numerical model was developed and validated to systematically investigate the effects of various heat and mass flow rates on key thermo-hydrodynamic characteristics, such as internal phase distribution and the occurrence of thermal non-equilibrium phenomena. This study provides key physical insights that can inform the design and optimization of advanced thermal protection systems for future reusable space vehicles.

2. Numerical methods

2.1. Governing equations

The Two-Phase Mixture Model (TPMM) originally proposed by Wang and Beckermann [18] was selected as the baseline model in this study. A limitation of the original TPMM is its reliance on the Local Thermal Equilibrium (LTE) assumption, which makes it unsuitable for phase change phenomena where evident temperature differences exist between the solid and fluid phases. Therefore, the present work adopts the Local Thermal Non-Equilibrium (LTNE) approach, based on the model developed by Shi and Wang [23]. Therefore, the resulting LTNE-TPMM is described by the following four conservation equations:

$$\nabla \cdot (\rho \vec{u}) = 0 \tag{1}$$

$$\rho \vec{u} = -\frac{K}{\nu(s)} \nabla P \tag{2}$$

$$\nabla \cdot (\gamma_h \rho \vec{u} h_f) = \nabla \cdot (k_{f,eff} \nabla T_f) + \nabla \cdot (-D(s) h_{fg} \nabla s) + q_{sf}$$
(3)

$$\nabla \cdot (k_{seff} \nabla T_s) = q_{sf} \tag{4}$$

Eqs. 1–4 represent the conservation of continuity, momentum, fluid energy, and solid energy. Eq. 3 contains an advection term on the left side and three right-side terms representing heat conduction, energy diffusion by capillary pressure, and solid-fluid volumetric heat source.

For numerical stability, the fluid energy equation (Eq. 3) requires a specific reformulation. Its original advection term, when based on mixture enthalpy, is prone to convergence issues during phase change due to sharp change in fluid property. To resolve such issues, the fluid energy equation is reformulated using kinetic enthalpy, a formulation originally developed by Wang and Beckermann. Therefore, final forms of the fluid energy equation and kinetic enthalpy can be written as:

$$\nabla \cdot (\rho \vec{u} h_k) = \nabla \cdot (\Gamma \nabla h_k) + q_{sf} \tag{5}$$

$$h_{k} = \gamma_{h} h_{f} = \begin{cases} c_{p,l} T_{f}, & (h_{k} < h_{l,sat}) \\ \lambda_{l} h_{l} + \lambda_{v} h_{v} = h_{v,sat} - \lambda h_{fg}, & (h_{l,sat} < h_{k} < h_{v,sat}) \\ c_{p,v} (T_{f} - T_{sat}) + h_{v,sat} & (h_{k} > h_{v,sat}) \end{cases}$$
(6)

The effective diffusion coefficient is formulated under two specific conditions where $\nabla s = 0$ in single-phase regions and $\nabla T_f = 0$ in the two-phase region. This approach yields the following expression:

$$\Gamma = \begin{cases} \frac{k_{l,\text{eff}}}{c_{p,l}}, & (h_k < h_{l,\text{sat}}) \\ \frac{D(s)}{d\lambda/ds}, & (h_{l,\text{sat}} < h_k < h_{v,\text{sat}}) \\ \frac{k_{v,\text{eff}}}{c_{p,v}}, & (h_k > h_{v,\text{sat}}) \end{cases}$$

$$(7)$$

The properties of coolants (liquid and gas) and porous structures are summarised in Tables 1 and 2 respectively. The constitutive relations used in Eqs. 1–7 are described in Table 3.

Table 1. Thermodynamic properties of the coolant used in the numerical simulations [25, 26]

Property	Water liquid	Water vapor
Density (kg/m³)	960	Ideal gas law
Specific heat (J/kg·K)	4,210	2,029
Thermal conductivity (W/m·K)	0.68	-21.994433 + 0.11842T
Dynamic viscosity (kg/m·s)	$24.141\times 10^{247.8//(T-140)}$	-2.77567 + 0.04035T
Prandtl number	$\mu_l c_{p,l}/k_l$	0.984

Table 2. Physical properties of the porous structure used in the numerical simulations

Property	Solid (Hastelloy X)	
Density (kg/m³)	8,400	
Specific heat (J/kg·K)	625	
Thermal conductivity (W/m·K)	$a_0 + a_1T + a_2T^2 + a_3T^3$	
	$a_0 = -3.6779$, $a_1 = 5.5488 \times 10^{-2}$, $a_2 = -4.8215 \times 10^{-5}$, $a_3 = 1.9656 \times 10^{-8}$	
Porosity	0.315	
Particle diameter (m)	1×10^{-4}	
Permeability (m²)	8.69×10^{-13}	

Table 3. Constitutive relationships in LTNE-TPMM [18, 23, 25]

Variable	Expression	
Mixture density	$\rho = \rho_l s_l + \rho_{\nu} (1 - s_l)$	
Relative permeability	$k_{rl} = s_l^3$, $k_{rl} = (1 - s_l)^3$	
Mixture kinematic viscosity	$\nu = \frac{1}{k_{rl}/\nu_l + k_{rv}/\nu_v}$	
Relative mobility	$\lambda_l = \lambda = u k_{rl} / u_l$, $\lambda_v = 1 - \lambda = u k_{rv} / u_v$	
Mixture Darcian velocity	$ec{u} = (ho_l ec{u}_l + ho_{ u} ec{u}_{ u})/ ho$	
Mixture enthalpy	$h_f = (\rho_l s_l h_l + \rho_v (1 - s_l) h_v) / \rho$	
Advection coefficient	$\gamma_h = \frac{\frac{\rho_l h_{l,sat}}{\mu_l} k_{rl} + \frac{\rho_v h_{v,sat}}{\mu_v} k_{rv}}{\frac{\rho_l h_{l,sat}}{\mu} s_l + \frac{\rho_v h_{v,sat}}{\mu} (1 - s_l)}$	
Specific surface area	$\alpha_{sf} = 6(1-\varepsilon)/d_p$	
Convective heat transfer coefficient of packed bed [22]	$h_{si} = \left(\frac{k_i}{d_p}\right) \left(2.0 + 1.1Pr_i^{0.33}Re_i^{0.6}\right), \qquad i = l, v$	
Heat transfer of nucleate boiling	$q_{\text{boil}} = \alpha_{sf} \mu_l h_{fg} \left(\frac{g(\rho_l - \rho_v)}{\sigma} \right)^{0.5} \left(\frac{c_{p,l} (T_s - T_{\text{sat}})}{C_{sf} h_{fg} P r_l} \right)^3$	
Solid-fluid volumetric heat transfer in pore	$q_{sf} = \begin{cases} h_{sl}\alpha_{sf}(T_s - T_f), & T_f < T_{\text{sat}} \\ s_l q_{\text{boil}} + (1 - s_l)h_{sv}\alpha_{sf}(T_s - T_{\text{sat}}), & T_f = T_{\text{sat}} \\ h_{sv}\alpha_{sf}(T_s - T_f), & T_f > T_{\text{sat}} \end{cases}$	
Effective thermal conductivity	$k_{f,\mathrm{eff}} = \varepsilon k_f$, $k_{s,\mathrm{eff}} = (1 - \varepsilon)k_s$	
Mixture pressure	$\nabla P = \lambda \nabla P_l + (1 - \lambda) \nabla P_v$	
Capillary pressure	$P_c = P_v - P_l = \left(\frac{\varepsilon}{K}\right)^{1/2} \sigma J(s_l)$	
Capillary pressure function	$J(s_l) = 1.417(1 - s_l) - 2.120(1 - s_l)^2 + 1.263(1 - s_l)^3$	
Capillary diffusion coefficient	$D(s_l) = \frac{K}{v} \lambda (1 - \lambda) \nabla p_c = \frac{K}{v} \lambda (1 - \lambda) \left(\frac{\varepsilon}{K}\right)^{1/2} \sigma[-J'(s_l)]$	

2.2. Physical model and boundary conditions

Fig. 1 presents the physical model applied to numerically analyse the phase change phenomenon of liquid coolants within the porous structure of the transpiration cooling system. The heat flux generated during atmospheric reentry is applied to the top of a porous structure installed on the outer wall of the space vehicle. Coolant is then injected with temperature T_c and mass flow rate m_f in the opposite direction of heat input to achieve transpiration cooling. The porous plate, which has a diameter of 60 mm and a thickness of 8 mm, is sintered with a nickel-based alloy with an average diameter of 100 μ m. As water within the porous structure absorbs thermal energy and undergoes vaporization, three characteristic zones emerge: a subcooled liquid zone, an intermediate two-phase mixture zone, and a superheated vapor zone. The liquid-mixture interface is represented by y_1 , and the mixture-vapor interface by y_2 . The positions of these phase boundaries dynamically shift depending on the heat flux and coolant mass flow conditions.

Fig. 1 (b) shows the boundary conditions applied to the numerical model. At the cold-side inlet boundary (Γ_{inlet}), a constant coolant mass flux condition is imposed, and the coolant is injected from the bottom of the porous plate upwards. The energy boundary conditions are derived from the law of energy conservation, which accounts for both the enthalpy of the inflowing fluid from the coolant reservoir and the convective heat transfer at the lower surface of the plate.

$$m_f = \rho u|_{\Gamma_{inlet}} \tag{8}$$

$$k_{s,eff} \frac{\partial T_s}{\partial y} \Big|_{\Gamma_{inlet}} = h_c (T_s |_{\Gamma_{inlet}} - T_c)$$
(9)

$$m_f(h_f|_{\Gamma_{inlet}} - h_{f,reservoir}) = h_c(T_s|_{\Gamma_{inlet}} - T_c) + k_{f,eff} \frac{\partial T_f}{\partial y}|_{\Gamma_{inlet}}$$
(10)

where h_c and T_c are the convective heat transfer coefficient at the cold side and the coolant injection temperature, respectively.

At the hot-side outlet boundary (Γ_{outlet}), the pressure outlet is defined under atmospheric pressure conditions. The heat flux at the outlet boundary is modelled according to the approach of Su et al.[25], which assumes that the entire applied heat flux is absorbed by the solid matrix.

$$p|_{\Gamma_{outlet}} = p_{atm} \tag{11}$$

$$k_{s,eff} \frac{\partial T_s}{\partial y} \bigg|_{\Gamma_{outlet}} = q'' \tag{12}$$

$$k_{f,eff} \left. \frac{\partial T_f}{\partial y} \right|_{\Gamma_{outlet}} = 0 \tag{13}$$

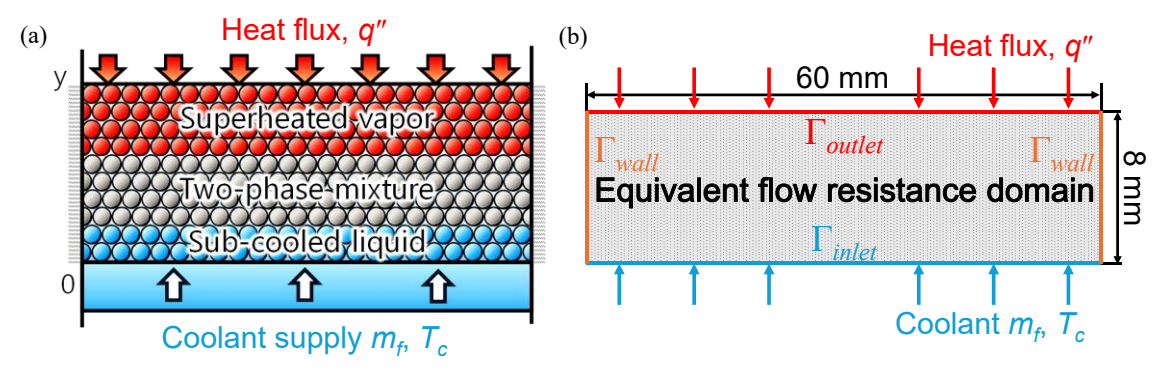


Fig 1. Physical model of transpiration cooling with phase change (a) multiphase flow regimes within the porous medium (b) computational domain and boundary conditions

2.3. Solution procedure

Computational simulations were conducted utilizing ANSYS Fluent 2022 R1, a commercial Finite Volume Method (FVM)-based solver. The governing equations for phase-change transpiration cooling were implemented using User-Defined Functions (UDFs). Continuity and momentum conservation within the porous medium were addressed using Fluent's integrated porous media modeling capabilities, whereas energy conservation for both solid and fluid phases was handled through custom User-Defined Scalar (UDS) transport equations. Given the inherently low mass flow rates and small length scales typical of transpiration cooling applications, the resulting Reynolds numbers justify the adoption of laminar flow assumptions. Pressure-velocity field coupling was achieved through the SIMPLE algorithm, while spatial discretization employed second-order upwind schemes for momentum and energy transport to maintain computational accuracy, with the PRESTO! scheme applied for pressure field discretization.

The coupled conservation equations are solved sequentially and iteratively using the following computational procedure. The flow and temperature fields are initially set to inlet velocity conditions and 300K for computational stability. In each iteration, the coolant phase (liquid, two-phase, vapor) is identified using enthalpy and pressure, followed by calculation of mixture properties and constitutive relations for each cell. The continuity and momentum equations yield updated pressure and velocity fields, while energy equations provide new enthalpy and solid temperature distributions. The iterative calculations are performed continuously until the residuals of the continuity and momentum equations fall below 10^{-6} and the residual of the energy equation falls below 10^{-8} .

2.4. Permeability

To measure the specimen's permeability, an experimental apparatus was developed that can deliver water at different flow rates while recording pressure differentials across the sample, as illustrated in Fig. 2(a). Two stainless steel housings clamp the specimen with 10 mm overlap on each side, exposing a 60 mm surface area. A chiller maintains coolant temperature at 300 K while a piston pump provides constant flow rates. Pressure sensors measure differential pressure across the specimen to characterize pressure drop versus flow velocity.

As shown in Fig. 2(b), the pressure drop exhibits a near-linear relationship with superficial velocity, characteristic of the Darcy flow regime. Using Darcy's law and the linear fitting slope, the specimen permeability was determined to be 8.69×10^{-13} m². The numerical model incorporating the derived permeability value was validated against experimental measurements. The results between experiments and simulations show excellent agreement, with a maximum error of only 90 Pa and an average relative error of 6.7%, validating the model's predictive capability.

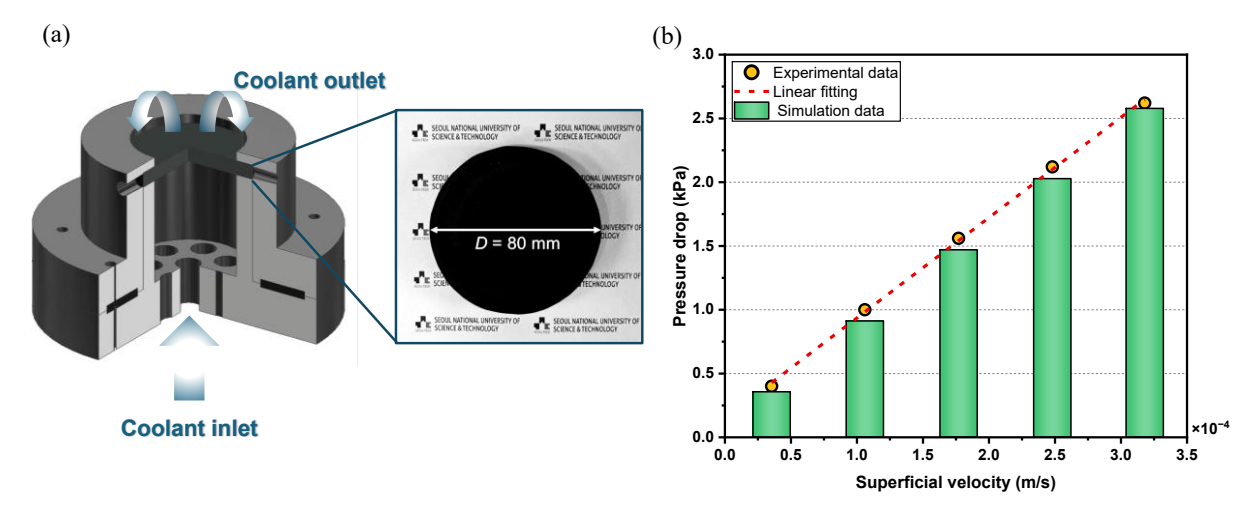


Fig 2. (a) Experimental setup to measure the specimen's permeability (b) relationship between superficial velocity and pressure drop, and comparison of numerical analysis results

3. Results and discussion

3.1. Validation of the numerical model

To assess the numerical model's accuracy in phase-change scenarios, its predictions were benchmarked against established studies by Shi and Wang [23] and Chen et al. [24]. The validation configuration features a porous medium with 0.01 m thickness, 0.3 porosity, and 20 µm mean particle size, subjected to 1.0 MW/m² heat flux from above and 0.5 kg/m²·s coolant injection from below. Fig. 3 presents a comparison of fluid temperature profiles along the flow direction between the current model and literature data. The current model's predictions align exceptionally well with the temperature trends reported in previous studies. Maximum relative deviations occur at the liquid-mixture interface, where the present model exhibits relative errors of 9.4% and 2.74% when compared to Shi and Wang [23] and Chen et al. [24] results, respectively. Despite these localized discrepancies, the overall agreement is deemed excellent, thereby substantiating the numerical model's reliability.

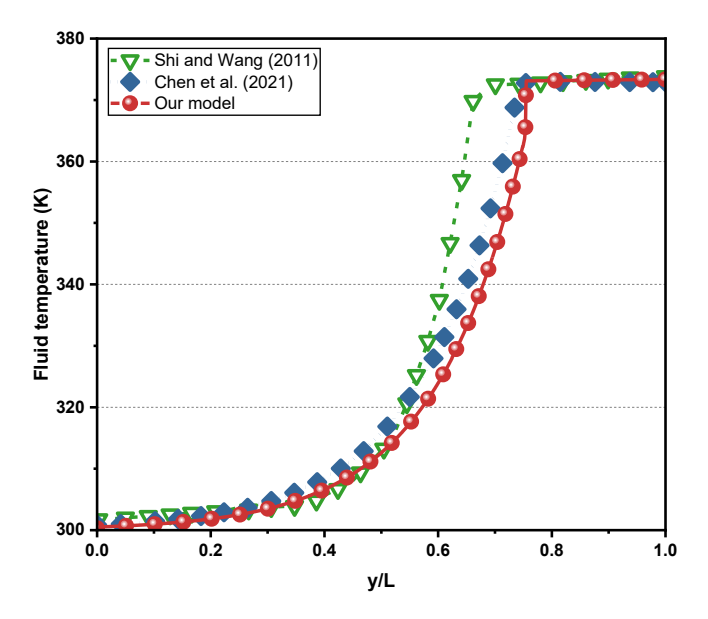


Fig 3. Validation of temperature profiles along the flow direction against results reported in previous studies [23, 24]

3.2. Liquid saturation field

Fig. 4 visually presents the evolution of phase distribution within the porous plate as the coolant mass flux is varied under two different heat flux conditions. Each contour clearly illustrates the spatial development of the liquid, two-phase mixture, and vapor regions as the coolant mass flux decreases. Under low heat flux conditions ($q'' = 0.2 \text{ MW/m}^2$), a gradual phase transition is observed. At a high mass flux (0.70 kg/m²·s), the porous medium is predominantly filled with liquid due to sufficient cooling capacity. As the flow rate decreases, the two-phase region gradually expands. However, even at the lowest flow rate (0.10 kg/m²·s), complete vaporization is effectively suppressed, indicating that stable two-phase cooling is maintained. In contrast, under high heat flux conditions ($q'' = 1.0 \text{ MW/m}^2$), rapid vapor formation occurs at the heated surface with a distinct vapor region begins to form at a much higher mass flux (0.325 kg/m²·s), indicating that intense external thermal energy causes instant coolant vaporization.

These qualitative observations from Fig. 4 are clearly substantiated by the quantitative data in Fig. 5, which tracks the precise locations of the phase change interfaces and the thickness of the two-phase region. The data numerically confirms that under low heat flux, a thick and stable two-phase zone is formed due to insufficient thermal energy for complete vaporization. In contrast, under high heat flux, the data clearly shows that convective heat transfer dominates over the capillary-driven liquid supply due to the intense thermal load. This results in early vapor formation and a very thin two-phase region.

HiSST-2025-167 Page | 7 Numerical Investigation of Heat Transfer and Flow Characteristics in Phase-Change

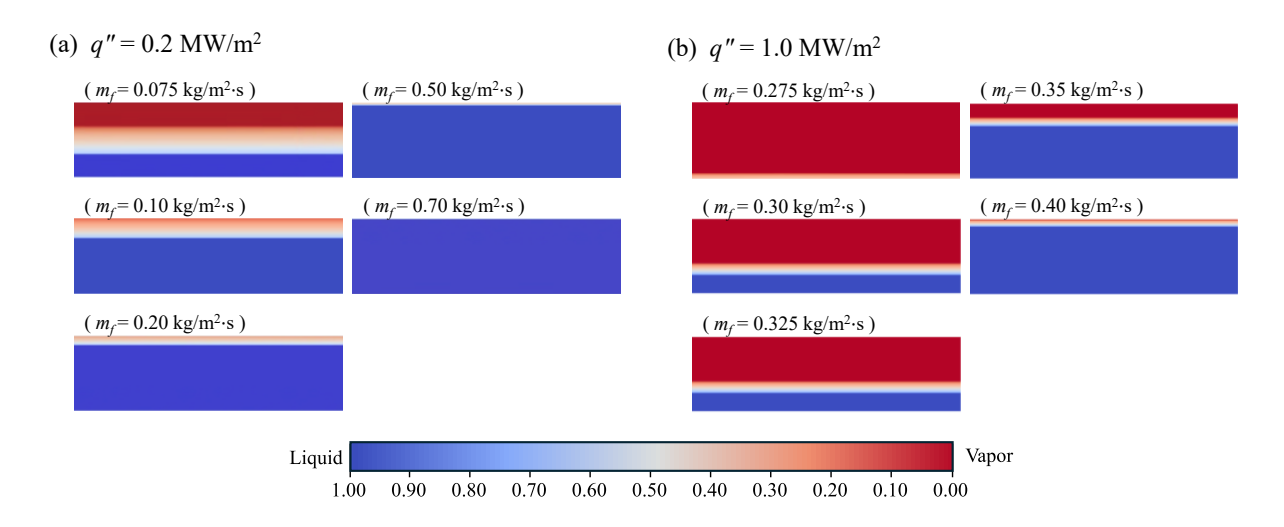


Fig 4. Liquid saturation distributions at different coolant mass fluxes under (a) $q'' = 0.2 \text{ MW/m}^2$ and (b) $q'' = 1.0 \text{ MW/m}^2$

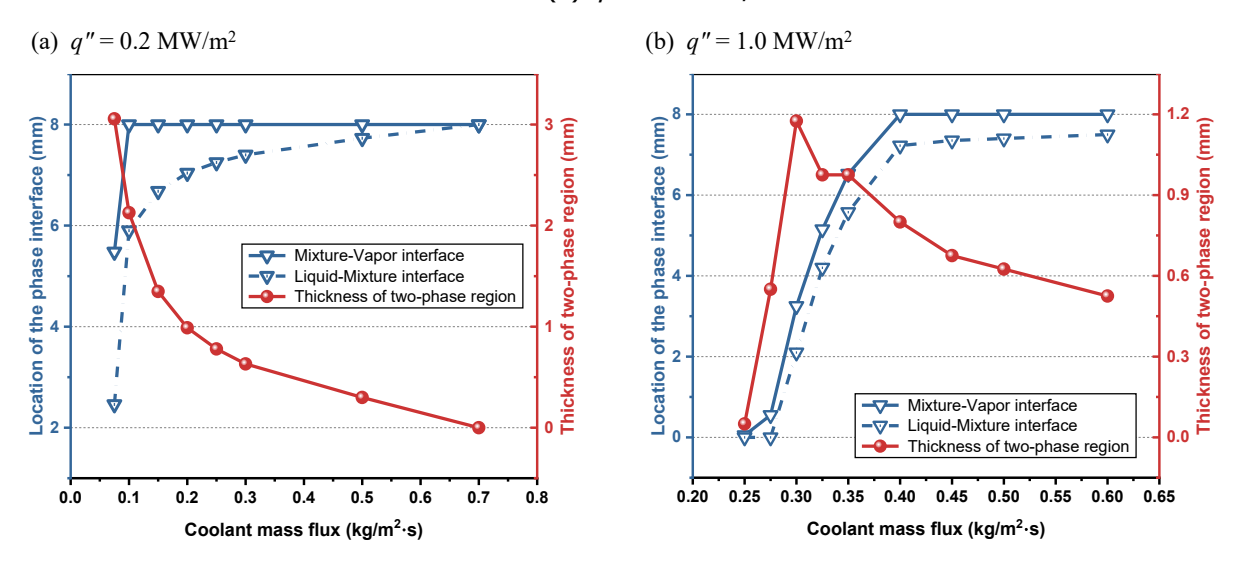


Fig 5. Variations of location of the phase-change interfaces and thickness of the two-phase region at different coolant mass fluxes under (a) $q'' = 0.2 \text{ MW/m}^2$ and (b) $q'' = 1.0 \text{ MW/m}^2$

3.3. Temperature Field and Local Thermal Non-Equilibrium Characteristics

Fig. 6 presents the distributions of temperature field within the porous plate as the coolant mass flux is varied under two different heat flux conditions. Corresponding to the liquid saturation distribution, the temperature profile is distinguished by three characteristic zones, each exhibiting distinct gradients and solid-fluid temperature differences. The vapor region exhibits a much steeper temperature gradient than the liquid region, primarily because the lower thermal conductivity of the vapour phase necessitates a greater gradient to maintain an equivalent heat transfer rate.

At low coolant flow rates, the expanded superheated vapor region causes higher surface temperatures exceeding the phase change layer, which maintained at saturation temperature. However, the temperature gradient within the vapor region becomes steeper under higher flow conditions. This occurs because higher vapor temperatures at low flow rates promote increased molecular activity and collision frequency, enhancing thermal conductivity and allowing for gentler temperature gradients. Conversely, higher flow rates create more effective cooling that reduces vapor temperatures, thereby decreasing thermal conductivity and necessitating steeper gradients to maintain the same heat transfer rate through the compressed vapor zone.

As visualized in the magnified inset of Fig. 6, Local Thermal Non-Equilibrium (LTNE) is a prominent feature of the temperature distribution during transpiration cooling. The single-phase region exhibits

almost complete thermal equilibrium between solid and fluid phases. In contrast, the two-phase region exhibits a distinct temperature difference, with the fluid temperature remaining fixed at saturation while the solid matrix continues to heat up due to the boiling process.

At low heat flux conditions, the coolant injection rate influences the temperature distribution within the liquid region. A higher mass flow rate promotes convective heat transfer, inducing an exponential temperature rise from the inlet (300K) to the saturation point (373.15K). Consequently, the coolant penetrates deeply into the hot side of the porous structure, maintaining a low temperature down to the interface where phase change occurs. Therefore, the cooling effect is concentrated near the coolant inlet, whilst simultaneously a steep temperature gradient appears at the interface. Moreover, the low heat flux causes insufficient thermal energy input to induce immediate vaporization of the coolant supplied by capillary action, leading instead to gradual phase change over a larger volume and creating a broad two-phase region.

Comparing representative low heat flux cases ($q''=0.2 \text{ MW/m}^2$, $m_f=0.075 \text{ kg/m}^2\text{s}$) and high heat flux cases ($q'''=1.0 \text{ MW/m}^2$, $m_f=0.30 \text{ kg/m}^2\text{s}$ and $0.325 \text{ kg/m}^2\text{s}$) exhibiting similar temperature distributions, it is observed that as the heat flux increases, the temperature in the hot side rises while the temperature in the cold side decreases. The increased thermal load necessitates higher flow rates, which shortens the phase change region and extends the single-phase regions. Consequently, in the vapor region, a steep temperature rise occurs due to the high heat flux, while in the liquid region, a temperature decrease occurs due to convection with the coolant at an injection temperature of 300K.

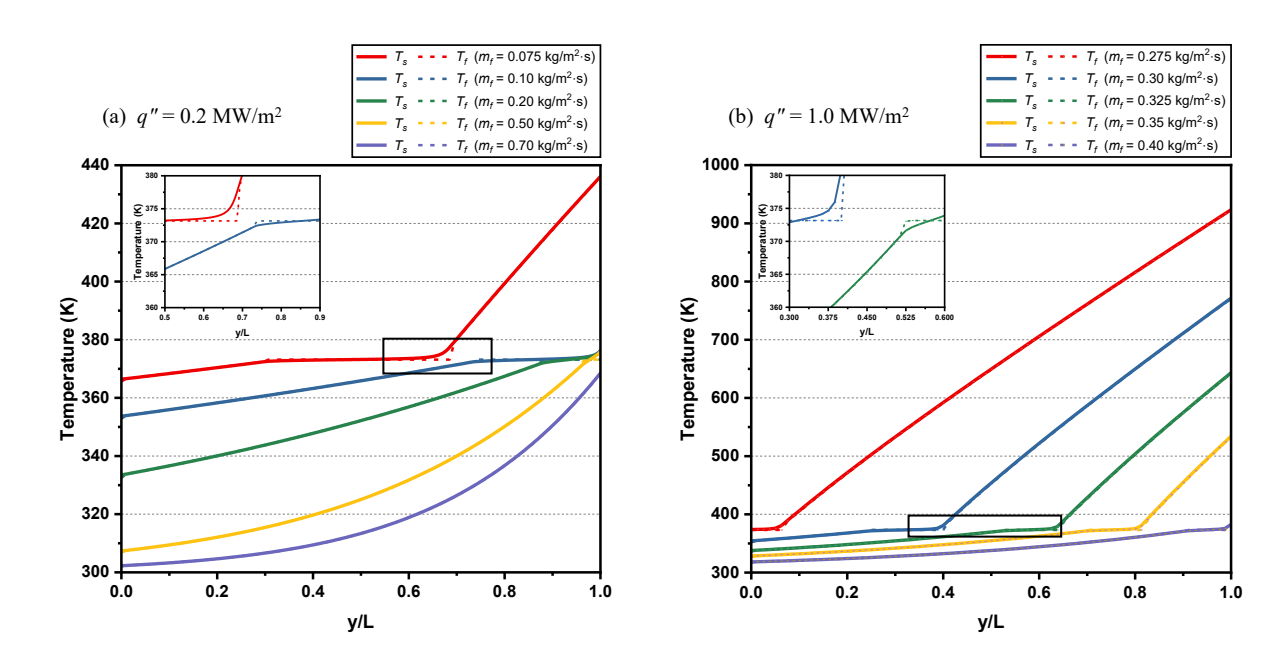


Fig 6. Temperature distributions along flow direction at different coolant mass fluxes under (a) $q'' = 0.2 \text{ MW/m}^2$ and (b) $q'' = 1.0 \text{ MW/m}^2$

3.4. Pressure drop

The relationship between coolant mass flux, pressure drop, and average kinematic viscosity is presented in Fig. 7. A distinct transition point appears where both pressure and the kinematic viscosity change abruptly. In the low flow rate region prior to the transition point, both the pressure drop and the average kinematic viscosity exhibit a distinct downward trend as the mass flow rate increases. Note that this is due to insufficient cooling, resulting in a greater proportion of vapor possessing relatively high kinematic viscosity. Subsequently, as the coolant flow rate increases, vapor generation is suppressed, leading to reduction of overall average kinematic viscosity. From Darcy's law (Eq. 2), the pressure drop is both proportional to the mass flow rate and the kinematic viscosity. In the low-flow region, even as flow rate increases, the effect of viscosity reduction due to decreased vapor fraction is greater. Therefore, contrary to common expectations, pressure drop decreases at higher flow rates.

HiSST-2025-167 Page | 9 Numerical Investigation of Heat Transfer and Flow Characteristics in Phase-Change

On the other hand, in the high-flow range, the system largely remains in a liquid state, exhibiting a low and constant average kinematic viscosity. Consequently, the influence of viscosity becomes negligible, resulting in the typical pattern where the pressure drop increases proportionally with flow rate.

Fig. 8 illustrates the local pressure distribution at different flow rates. In most cases, the pressure gradient is gentle in the single-phase liquid region near the inlet. However, when phase change occurs, the pressure gradient increases sharply due to the formation of high-viscosity vapor. Interestingly, at the highest flow rates (0.50, 0.70 kg/m²·s), the initial pressure gradient is steeper than at some lower flow rates. High coolant flow rate effectively suppresses the inlet temperature, which increases the kinematic viscosity of liquid water. Since Darcy's law dictates that pressure drop is proportional to both viscosity and mass flux, the elevated viscosity of the cold liquid becomes the dominant factor responsible for the steeper initial pressure gradient observed in the all-liquid zone.

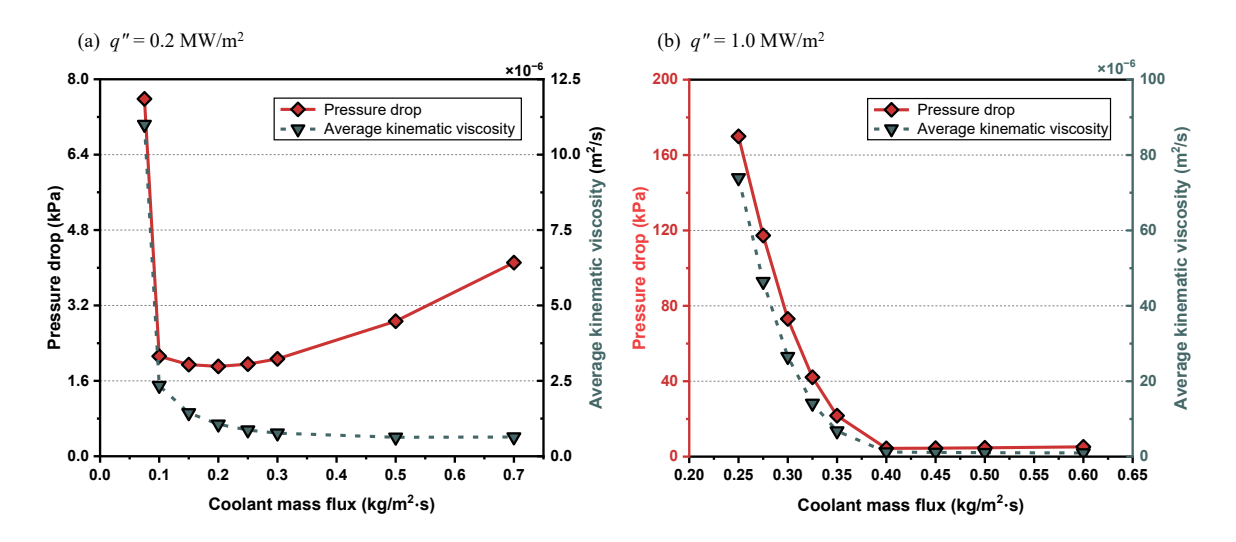


Fig 7. The variations in pressure drop and average kinematic viscosity at different coolant mass fluxes under (a) $q'' = 0.2 \text{ MW/m}^2$ and (b) $q'' = 1.0 \text{ MW/m}^2$

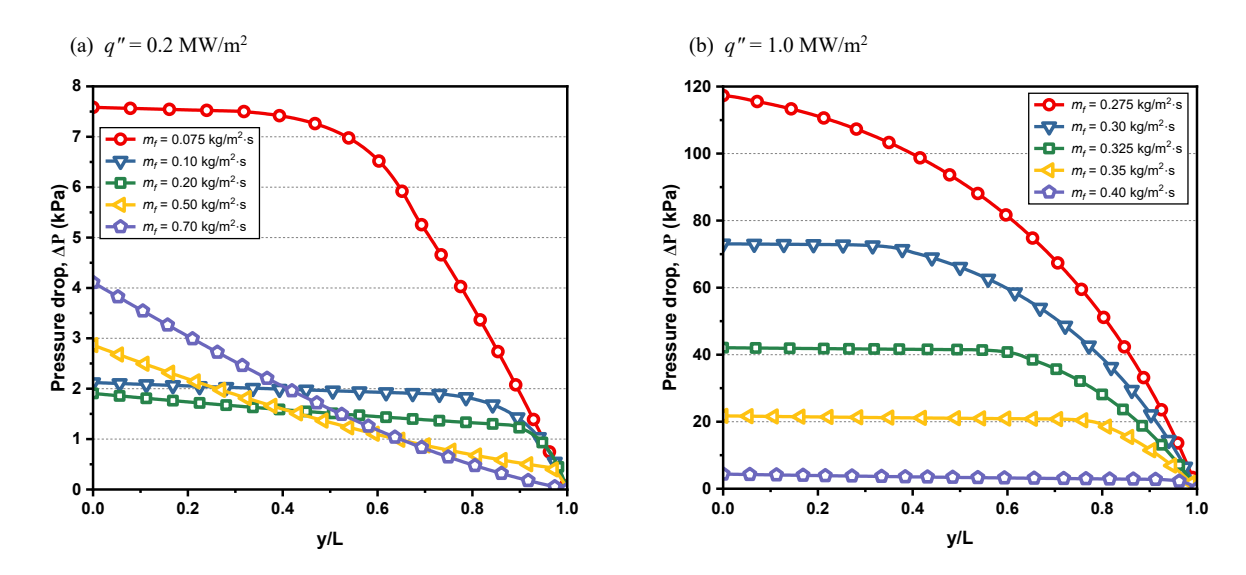


Fig 8. Pressure distributions along flow direction at different coolant mass fluxes under (a) q'' = 0.2 MW/m² and (b) q'' = 1.0 MW/m²

4. Conclusion

In this study, numerical investigation was conducted to analyse the internal flow and heat transfer within a phase change transpiration cooling system for active thermal protection of re-entry space vehicle. A numerical analysis model was developed to predict the temperature and pressure within the system based on the heat flux applied to the vehicle during re-entry and the coolant flow rate. By systematically analysing the phase distribution, temperature field, local thermal non-equilibrium phenomena, and pressure drop behaviour within the porous medium, the following conclusions were drawn:

- The numerical model demonstrated excellent accuracy in predicting phase-change transpiration cooling, with maximum relative errors of 9.4% when compared to established studies. The strong agreement with literature data substantiates the model's reliability for analyzing complex phase-change phenomena in porous media cooling systems.
- The study revealed distinct operating regimes governed by heat flux intensity. Under low heat flux conditions (q" = 0.2 MW/m²), gradual phase transitions occur with stable two-phase cooling maintained even at low flow rates. Conversely, high heat flux conditions (q" = 1.0 MW/m²) induce rapid vapor formation and thin two-phase regions due to convective heat transfer dominance. Local Thermal Non-Equilibrium (LTNE) effects are prominent in two-phase regions, where fluid temperatures remain at saturation while solid matrix continue heating during boiling processes.
- This study has clarified the mechanism behind the negative pressure gradient observed at low mass flow rates. Analysis confirmed that within the evaporation-dominated regime, the pressure drop is governed not by increasing mass flow rates, but by a far more pronounced decrease in the average kinematic viscosity due to vapour suppression. This interaction between mass flow rate and the viscosity reduction caused by phase change is a key characteristic of the fluid dynamic behaviour in this system.

Acknowledgments

This work was supported by the "A nature-inspired high-efficiency solar energy collector mimicking energy metabolic mechanism of plants" funded by the National Research Foundation (NRF, 2022R1C1C1005922), Republic of Korea, and this work was also supported by Korea Research Institute for defense Technology planning and advancement(KRIT) grant funded by the Korea government (DAPA(Defense Acquisition Program Administration)) (No.KRIT-CT-22-030, Reusable Unmanned Space Vehicle Research Center, 2025).

References

- 1. Jones, Harry.: The recent large reduction in space launch cost. 48th International Conference on Environmental Systems, (2018)
- 2. Anderson, John David.: Hypersonic and high temperature gas dynamics (1989)
- 3. Fu, L., Karp, M., Bose, S. T., Moin, P., Urzay, J.: Shock-induced heating and transition to turbulence in a hypersonic boundary layer. Journal of Fluid Mechanics 909 (2021). https://doi.org/10.1017/jfm.2020.935
- 4. Uyanna, Obinna, Hamidreza Najafi.: Thermal protection systems for space vehicles: A review on technology development, current challenges and future prospects. Acta Astronautica 176, 341-356. (2020). https://doi.org/10.1016/j.actaastro.2020.06.047
- 5. Naebe, M., Abolhasani, M. M., Khayyam, H., Amini, A., Fox, B.: Crack damage in polymers and composites: A review. Polymer reviews, 56(1), 31-69. (2016). https://doi.org/10.1080/15583724.2015.1078352
- 6. Xu, H., Su, R., He, Y., Zhang, X., Hu, C., Tang, D.: Research progress on the failure modes and failure mechanisms of the transpiration cooling structure. International Communications in Heat and Mass Transfer, 167, 109399. (2025). https://doi.org/10.1016/j.icheatmasstransfer.2025.109399
- 7. Yinhai, Z. H. U., Wei, P. E. N. G., Ruina, X. U.: Review on active thermal protection and its heat transfer for airbreathing hypersonic vehicles. Chinese Journal of Aeronautics, 31(10), 1929-1953. (2018). https://doi.org/10.1016/j.cja.2018.06.011

- 8. Wang, W., Yan, Y., Zhou, Y., Cui, J.: Review of advanced effusive cooling for gas turbine blades. Energies, 15(22), 8568. (2022). https://doi.org/10.3390/en15228568
- 9. Mi, Q., Yi, S. H., Gang, D. D., Lu, X. G., Liu, X. L.: Research progress of transpiration cooling for aircraft thermal protection. Applied Thermal Engineering, 236, 121360. (2024). https://doi.org/10.1016/j.applthermaleng.2023.121360
- 10. Liu, Y. Q., Jiang, P. X., Jin, S. S., Sun, J. G.: Transpiration cooling of a nose cone by various foreign gases. International journal of heat and mass transfer, 53(23-24), 5364-5372. (2010). https://doi.org/10.1016/j.ijheatmasstransfer.2010.07.019
- 11. van Foreest, A., Sippel, M., Gülhan, A., Esser, B., Ambrosius, B. A. C., Sudmeijer, K.: Transpiration cooling using liquid water. Journal of Thermophysics and Heat Transfer, 23(4), 693-702. (2009). https://doi.org/10.2514/1.39070
- 12. Wang, J., Zhao, L., Wang, X., Ma, J., Lin, J.: An experimental investigation on transpiration cooling of wedge shaped nose cone with liquid coolant. International Journal of Heat and Mass Transfer, 75, 442-449. (2014). https://doi.org/10.1016/j.ijheatmasstransfer.2014.03.076
- 13. Shen, L., Wang, J., Dong, W., Pu, J., Peng, J., Qu, D., Chen, L.: An experimental investigation on transpiration cooling with phase change under supersonic condition. Applied Thermal Engineering, 105, 549-556. (2016). https://doi.org/10.1016/j.applthermaleng.2016.03.039
- 14. Shin, J., Bae, J., Kim, S. J., Kim, T. Y.: Flow regimes and flow instability of transpiration cooling. International Journal of Heat and Mass Transfer, 252, 127457. (2025). https://doi.org/10.1016/j.ijheatmasstransfer.2025.127457
- 15. Zhu, P. F., Xue, Z. R., Qin, F., He, G. Q., Li, W. Q.: "Vapor blockage" and aqueous oxidation in C/SiC porous ceramic during transpiration cooling with phase change. International Journal of Heat and Mass Transfer, 242, 126842. (2025). https://doi.org/10.1016/j.ijheatmasstransfer.2025.126842
- 16. Dastvareh, B., Azaiez, J.: Instabilities of nanofluid flow displacements in porous media. Physics of Fluids, 29(4). (2017). https://doi.org/10.1063/1.4978890
- 17. He, F., Wang, J., Xu, L., Wang, X.: Modeling and simulation of transpiration cooling with phase change. Applied Thermal Engineering, 58(1-2), 173-180. (2013). https://doi.org/10.1016/j.applthermaleng.2013.04.017
- 18. Chao-Yang, W., Beckermann, C.: A two-phase mixture model of liquid-gas flow and heat transfer in capillary porous media—I. Formulation. International journal of heat and mass transfer, 36(11), 2747-2758. (1993). https://doi.org/10.1016/0017-9310(93)90094-M
- 19. Huang, Z., Zhu, Y. H., Xiong, Y. B., Jiang, P. X.: Investigation of transpiration cooling for sintered metal porous struts in supersonic flow. Applied thermal engineering, 70(1), 240-249. (2014). https://doi.org/10.1016/j.applthermaleng.2014.02.076
- 20. Xu, R., Huang, Y., Jiang, P., Wang, B.: Internal heat transfer coefficients in microporous media with rarefaction effects. Science China Technological Sciences, 55(10), 2869-2876. (2012). https://doi.org/10.1007/s11431-012-4994-3
- 21. Nield, D. A., Kuznetsov, A. V., Xiong, M.: Effect of local thermal non-equilibrium on thermally developing forced convection in a porous medium. International Journal of Heat and Mass Transfer, 45(25), 4949-4955. (2002). https://doi.org/10.1016/S0017-9310(02)00203-X
- 22. Wakao, N., Kaguei, S., Funazkri, T.: Effect of fluid dispersion coefficients on particle-to-fluid heat transfer coefficients in packed beds: correlation of Nusselt numbers. Chemical engineering science, 34(3), 325-336. (1979). https://doi.org/10.1016/0009-2509(79)85064-2
- 23. Shi, J. X., Wang, J. H.: A numerical investigation of transpiration cooling with liquid coolant phase change. Transport in porous media, 87(3), 703-716. (2011). https://doi.org/10.1007/s11242-010-9710-9
- 24. Chen, Y., Du, S., Li, D., Gao, Y., He, Y. L.: Numerical investigation of transient phase-change transpiration cooling based on variable properties of coolant. Applied Thermal Engineering, 184, 116204. (2021). https://doi.org/10.1016/j.applthermaleng.2020.116204
- 25. Su, H., Wang, J., He, F., Chen, L., Ai, B.: Numerical investigation on transpiration cooling with coolant phase change under hypersonic conditions. International Journal of Heat and Mass Transfer, 129, 480-490. (2019). https://doi.org/10.1016/j.ijheatmasstransfer.2018.09.123
- 26. Liu, T., Su, H., Chen, Z., He, F., Wang, J.: Numerical investigation on the transient transport and heat transfer characteristics of transpiration cooling with liquid phase change during coolant adjustment. Applied Thermal Engineering, 209, 118277. (2022). https://doi.org/10.1016/j.applthermaleng.2022.118277